

Delocalization and re-entrant localization of flat-band states in non-Hermitian disordered lattice models with flat bands

Sangbum Kim¹ and Kihong Kim^{2,3}

¹*Research Institute for Basic Sciences, Ajou University, Suwon 16499, Korea*

**E-mail: sangbumkim@ajou.ac.kr*

²*Department of Physics, Ajou University, Suwon 16499, Korea*

**E-mail: khkim@ajou.ac.kr*

³*School of Physics, Korea Institute for Advanced Study, Seoul 02455, Korea*

.....
 We present a numerical study of Anderson localization in disordered non-Hermitian lattice models with flat bands. Specifically we consider one-dimensional stub and two-dimensional kagome lattices that have a random scalar potential and a uniform imaginary vector potential and calculate the spectra of the complex energy, the participation ratio, and the winding number as a function of the strength of the imaginary vector potential, h . The flat-band states are found to show a double transition from localized to delocalized and back to localized states with h , in contrast to the dispersive-band states going through a single delocalization transition. When h is sufficiently small, all flat-band states are localized. As h increases above a certain critical value h_1 , some pair of flat-band states become delocalized. The participation ratio associated with them increases substantially and their winding numbers become nonzero. As h increases further, more and more flat-band states get delocalized until the fraction of the delocalized states reaches a maximum. For larger h values, a re-entrant localization takes place and, at another critical value h_2 , all flat-band states return to compact localized states with very small participation ratios and zero winding numbers. This re-entrant localization transition, which is due to the interplay among disorder, non-Hermiticity, and flat band, is a phenomenon occurring in many models having an imaginary vector potential and a flat band simultaneously. We explore the spatial characteristics of the flat-band states by calculating the local density distribution.

Subject Index 150 Disordered systems, Anderson transitions, 19 Low dimensional systems - electronic properties

1 Introduction

Even though Anderson localization of quantum particles and classical waves in random media has been studied extensively for over six decades [1–5], many aspects of it are not yet fully understood and localization phenomena with qualitatively new characteristics are still being discovered when adding new ingredients to the model [6–12]. In this paper, we explore a novel type of Anderson localization that occurs when the system is non-Hermitian and has a dispersionless flat band in its energy spectrum at the same time.

Non-Hermiticity can be introduced into the model in various ways such as adding an imaginary scalar or vector potential [13, 14]. The localization-delocalization transition in one- and two-dimensional lattice models with a random real scalar potential and a constant imaginary vector potential has been studied extensively since first being proposed by Hatano and Nelson [15–21]. Here we generalize such studies to the lattices supporting a flat band. There has been substantial recent interest in the properties of electronic and photonic systems with flat bands [22–25]. In those systems, the group velocity associated with the flat band vanishes which causes many interesting phenomena to occur by enhancing the effects of various perturbations including disorder [26–31]. Two-dimensional (2D) lattices such as the Lieb, dice, and kagome lattices and one-dimensional (1D) lattices such as the stub, sawtooth, and diamond lattices are among the representative examples exhibiting flat bands [32–35]. Our main aim in this paper is to investigate the influence of non-Hermiticity due to the imaginary vector potential \mathbf{g} on the localization of the flat-band states. Especially we will demonstrate that as the strength of \mathbf{g} increases, a substantial portion of those states go through a double transition from localized to delocalized and then back to localized states. This type of re-entrant localization transition has never been studied previously.

2 Model and method

We generalize the Hatano-Nelson model to the cases with a flat band such as the stub lattice, a schematic of which is shown in Fig. 1. We notice that a unit cell of the stub lattice consists of three inequivalent sites, A, B, and C. The stationary discrete Schrödinger equation

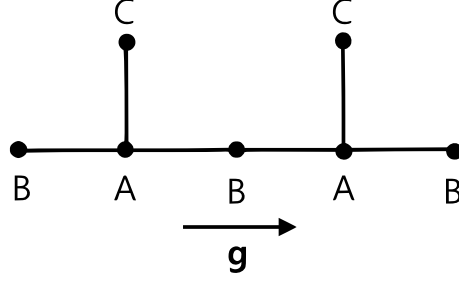


Fig. 1 Sketch of the stub lattice. The direction of the imaginary vector potential \mathbf{g} is indicated with an arrow.

for the stub lattice can be written as

$$\begin{aligned}
 E_\lambda \psi_\lambda(A, n) &= v_n^A \psi_\lambda(A, n) + te^h \psi_\lambda(B, n-1) \\
 &\quad + te^{-h} \psi_\lambda(B, n) + t \psi_\lambda(C, n), \\
 E_\lambda \psi_\lambda(B, n) &= v_n^B \psi_\lambda(B, n) + te^h \psi_\lambda(A, n) \\
 &\quad + te^{-h} \psi_\lambda(A, n+1), \\
 E_\lambda \psi_\lambda(C, n) &= v_n^C \psi_\lambda(C, n) + t \psi_\lambda(A, n),
 \end{aligned} \tag{1}$$

where $\psi_\lambda(m, n)$ ($m = A, B, C$) represents the eigenfunction at the n -th unit cell and E_λ is the (complex) energy eigenvalue. v_n^m is an on-site random potential chosen from the uniform distribution in $[-\Delta, \Delta]$. If we assume \mathbf{g} to have the dimension of momentum, then the dimensionless non-Hermiticity parameter h is defined by $h = ga/\hbar$, where a is the lattice spacing. te^h and te^{-h} represent the asymmetric nearest-neighbor hopping integrals between the A and B sites.

We apply the periodic boundary condition to a stub lattice with total unit cell number N_c and total site number $N (= 3N_c)$ and solve the eigenvalue problem given by Eq. (1). Since the system is non-Hermitian, we need to calculate both the *normalized* left and right eigenfunctions $\psi_\lambda^L(m, n)$ and $\psi_\lambda^R(m, n)$ corresponding to the same eigenvalue E_λ , using which we compute the participation ratio P_λ defined by

$$P_\lambda = \frac{1}{\sum_m \sum_{n=1}^{N_c} |\psi_\lambda^L(m, n) \psi_\lambda^R(m, n)|^2}. \tag{2}$$

We note that P_λ is bounded by $1 \leq P_\lambda \leq N$.

Next we calculate the winding number W_λ , which is defined in the same way as in [17, 18]:

$$W_\lambda = \frac{1}{2\pi} \oint_{C_0} d\alpha_\lambda, \tag{3}$$

where α_λ is the site-dependent phase of the eigenfunction and C_0 is a closed contour surrounding the origin of the complex plane. When the eigenvalue E_λ is complex, the eigenfunctions $\psi_\lambda^R(m, n)$ and $\psi_\lambda^L(m, n)$ rotate (in the opposite directions) an integer times around the origin on the complex plane, as the closed contour is traversed once. In actual calculations, we choose any closed contour around a ring of the stub lattice (satisfying the periodic boundary condition) and sum the phase of the eigenfunction $\psi_\lambda^R(m, n)$ [or equivalently $\psi_\lambda^L(m, n)$] at every site on the contour and divide the result by 2π , when the phase at a reference site is fixed to zero. Among many possible contours, we choose the simplest one traversing only the A and B sites. The present winding number, which is well-defined even in strongly disordered cases, is the generalization for non-Hermitian disordered systems of the wave vectors labelling the eigenstates in non-disordered systems. This quantity needs to be distinguished from the winding number describing the vorticity of complex energy eigenvalues [36, 37].

The spectrum of a clean stub lattice (i.e., $\Delta = 0$) with an imaginary vector potential h is given by

$$E_\lambda = \begin{cases} \pm \sqrt{3 + 2 \cosh(2h - iq_\lambda)} \\ 0 \end{cases}, \quad (4)$$

where $q_\lambda (= 2\pi\lambda/N_c, \lambda = 1, 2, \dots, N_c)$ is a wave vector in the first Brillouin zone [23]. It consists of a highly degenerate flat band with N_c states at $E_\lambda = 0$ and either two separate dispersive bands each with N_c states (for $h \lesssim 0.48$) or one merged dispersive band with $2N_c$ states (for $h \gtrsim 0.48$). The (unnormalized) flat-band eigenfunction is a compact localized state in which it is nonzero only at three adjacent sites

$$\begin{aligned} \psi_\lambda(\text{C}, n) &= e^{-h}, \quad \psi_\lambda(\text{C}, n+1) = e^h, \\ \psi_\lambda(\text{B}, n) &= -1. \end{aligned} \quad (5)$$

We note that $P_\lambda = 3$ when $h = 0$ and $P_\lambda \approx 1$ when h is large. When weak disorder is turned on, the clear distinction between flat and dispersive bands is maintained except in the very narrow transition region near and slightly below $h = 0.48$. In such cases, we define P_{FB} as the participation ratio averaged over N_c flat-band states and P_{av} as that averaged over all N states. We also consider many independent disorder configurations with the same Δ and denote the ensemble average as $\langle \dots \rangle$.

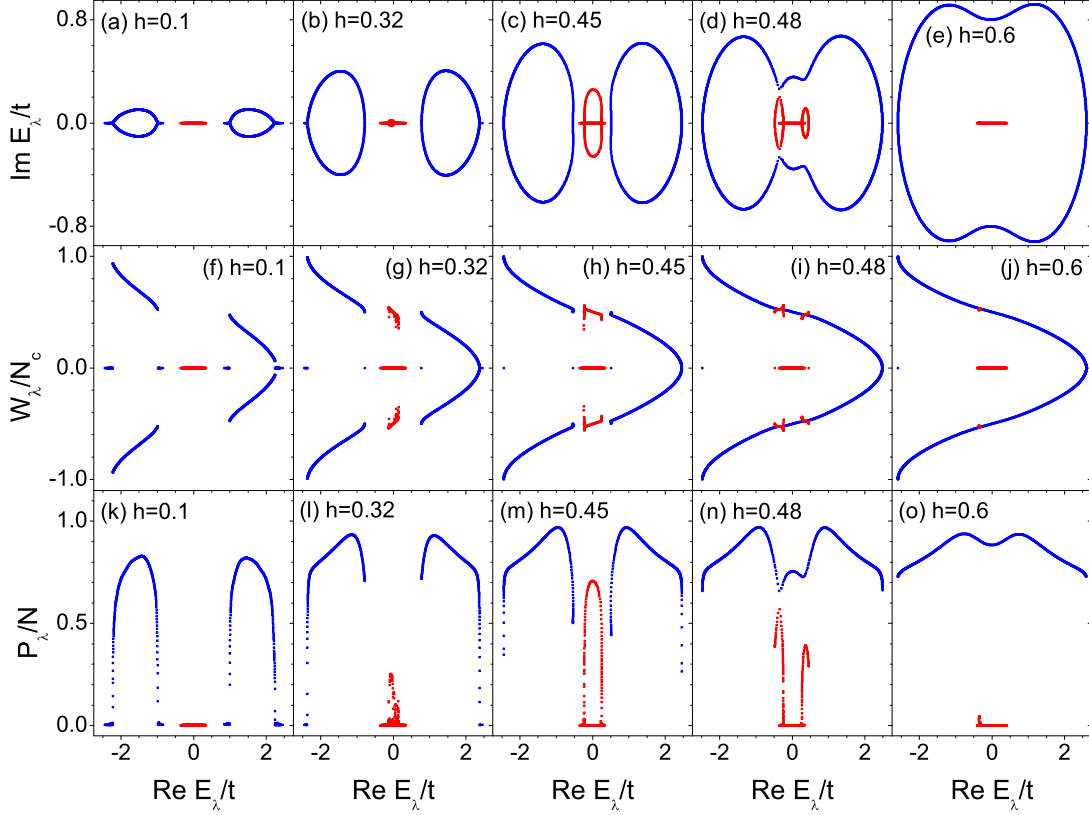


Fig. 2 (a-e) Complex energy spectra of a stub lattice in a single disorder configuration when $N_c = 800$, $N(= 3N_c) = 2400$, $\Delta/t = 0.4$, and $h = 0.1, 0.32, 0.45, 0.48, 0.6$. (f-j) Winding number W_λ divided by the total unit cell number N_c and (k-o) the participation ratio P_λ divided by the total site number N plotted versus the real part of the energy eigenvalue normalized by t . The blue (red) color corresponds to the dispersive bands (flat band) consisting of 1600 (800) states.

3 Numerical results

3.1 Stub lattice

In Fig. 2, we show our numerical results for the spectra of the energy eigenvalue, the winding number, and the participation ratio obtained for a stub lattice in a single disorder configuration, when $N_c = 800$, $\Delta/t = 0.4$, and $h = 0.1, 0.32, 0.45, 0.48, 0.6$. We plot the results for the flat band in red and those for the dispersive bands in blue. The flat-band states show markedly different behavior from the dispersive-band states. The evolution of the spectra for the dispersive bands with h when $h \lesssim 0.47$ is qualitatively similar to that for the

1D Hatano-Nelson model. When h is zero or sufficiently small, all states are localized with real energy eigenvalues and zero winding numbers. As h increases above a small critical value h_a , which is about 0.007 in the present disorder configuration, some states near the centers of the two dispersive bands get delocalized and their eigenvalues become complex. Delocalization always occurs for a pair of states with the eigenvalues being the complex conjugate of each other. When there are enough delocalized states, the plot of their eigenvalues in the complex plane takes the shape of a *bubble*. As h increases further above another critical value h_b (~ 0.45), all states in the dispersive bands become delocalized and their eigenvalues become complex except for those at the band edges. In Fig. 2(c), we note that two large (blue) bubbles corresponding to the two dispersive bands are formed.

When delocalization occurs for a pair of states, the winding number changes from zero to a pair of nonzero values with the same magnitude but of opposite sign. We observe that for dispersive-band states with nonzero W_λ , there is no degeneracy of W_λ and its absolute value is a monotonically decreasing function of $\text{Re } E_\lambda$. The values of $|W_\lambda|$ for the lower dispersive band are larger than those for the higher one. When all dispersive-band states are delocalized, the range of W_λ is $0 \leq |W_\lambda| \leq N_c - 1$. The winding numbers for all band-edge states remain zero. The participation ratios for most delocalized states are much larger than those for localized ones. The maximum of P_λ is approximately $0.97N$. This means that the most homogeneous delocalized state in the dispersive bands is the one spreading almost evenly over all lattice sites.

The evolution of the spectra for the flat band can be seen from the red-colored parts of Fig. 2. When h is smaller than h_1 , which is about 0.26 in the present configuration and much larger than h_a corresponding to the dispersive bands, all flat-band states are localized with real eigenvalues, zero winding numbers, and very small participation ratios of $P_\lambda \gtrsim 3$. As h increases above h_1 , some states near the center of the flat band get delocalized and their eigenvalues become complex, similarly to the dispersive-band case. Again, delocalization occurs for a pair of states with the eigenvalues being the complex conjugate of each other. As h increases further, the plot of the delocalized eigenvalues in the complex plane is characterized by a (red) bubble as in Fig. 2(c). However, unlike in the dispersive case where all states within the energy range of a bubble are delocalized, a majority of the states inside the range of a bubble remain localized in the flat-band case. Therefore the spectrum takes the shape of a *bubble pierced by the real line*. The fraction of delocalized states among all flat-band states is about 0.29 in Fig. 2(c). Most of the winding numbers for the delocalized states take the values close to $N_c/2$. We observe that for each of almost all the flat-band states with nonzero W_λ , there exists a dispersive-band state with the same winding number. Furthermore, there are a few cases where multiple flat-band states have the same winding

number. The participation ratios of delocalized flat-band states can be substantially large. We find that the maximum P_λ for the flat band is about $0.71N$, which implies that the most homogeneous delocalized state is the one spreading almost evenly over the two-thirds of the sites. We will show later in Fig. 5 that only the B and C sites are occupied in this case.

In the disorder configuration considered in Fig. 2, the flat- and dispersive-band states go through merging and decoupling in two steps within a very narrow range of h between 0.467 and 0.48, as shown in Fig. 3. More specifically, at $h \approx 0.468$, the flat-band bubble merges with the right dispersive-band bubble and then gets separated as a smaller bubble in the positive energy region when $h \approx 0.469$. At $h \approx 0.479$, another merging with the left dispersive-band bubble occurs and then the decoupling of the flat and dispersive bands is completed when $h \approx 0.48$, at which the flat-band spectrum consists of two bubbles connected by a real line as shown in Fig. 3(f). Above $h = 0.48$, the dispersive-band bubbles are merged into one big bubble and are separated from the flat band. The width of the region of h where the merging and decoupling occurs increases gradually as the disorder strength Δ increases. As h increases above 0.48, the effect of the imaginary vector potential begins to dominate the disorder effect and more and more states become re-localized with real eigenvalues, zero winding numbers, and very small participation ratios. At $h \approx 0.63$, all flat-band states return to compact localized states with $P_\lambda \approx 1$.

In order to show the double transition from localized to delocalized and back to localized flat-band states more explicitly, we plot $\langle P_{\text{FB}} \rangle / N$ and $\langle P_{\text{av}} \rangle / N$ obtained by averaging over 100 independent disorder configurations versus h , when $N = 2400$ and $\Delta/t = 0.1$ and 0.4 , in Fig. 4. The behavior of $\langle P_{\text{FB}} \rangle$ shows unambiguously the delocalization transition at $h = h_1$ and the re-entrant localization transition at $h = h_2$. For $h < h_1$, $\langle P_{\text{FB}} \rangle$ remains very close to 3 corresponding to a compact localized state at three adjacent B and C sites. For $h > h_2$, $\langle P_{\text{FB}} \rangle$ is close to 1 corresponding to a compact localized state at a single C site. Between h_1 and h_2 , $\langle P_{\text{FB}} \rangle$ increases rapidly, takes a maximum value near $h \approx 0.45$, and then decreases sharply to 1. The maximum of $\langle P_{\text{FB}} \rangle / N$ depends on the disorder and is about 0.12 when $\Delta/t = 0.4$. From Fig. 4(b), we find that the double transition of the flat-band states noticeably affects the shape of the $\langle P_{\text{av}} \rangle$ curve, which is characterized by the appearance of a distinct peak in the region between h_1 and h_2 , though its h dependence is not as dramatic as $\langle P_{\text{FB}} \rangle$.

In Fig. 5, we plot local density distributions for two typical dispersive-band and two typical flat-band states versus j , the odd [even] values of which correspond to the B (red) [A (green) and C (blue)] sites in the same disorder configuration as in Fig. 2, when $N_c = 800$, $\Delta/t = 0.4$, and $h = 0.45$. Figs. 5(b), (d), (f), and (h) are the magnified versions of (a), (c), (e), and (g) respectively. In the dispersive-band case, we find that the local density varies smoothly between A and B sites, while the density at the C sites either fluctuates more

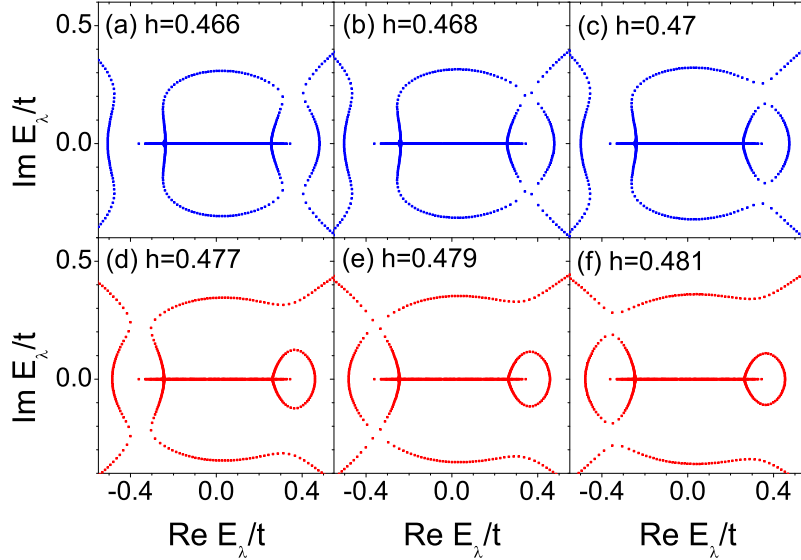


Fig. 3 Evolution of the complex energy spectrum of a stub lattice as h increases (a-c) from 0.466 to 0.47 and (d-f) from 0.477 to 0.481 in the same disorder configuration as in Fig. 2 when $N = 2400$ and $\Delta/t = 0.4$.

strongly than or shows a different spatial dependence from those at the A and B sites. In the flat-band case, the local density at the A sites always remains extremely small, while those at the B and C sites are sizable. For the flat-band states with large participation ratios such that $P_\lambda/N \approx 0.7$, all B and C sites are roughly equally populated. For those with small participation ratios, only a small number of C sites are substantially occupied as shown in Fig. 5(h). These behaviors can be understood from the fact that the wave functions for the flat-band states are obtained approximately by a superposition of the functions given by Eq. (5) for many different n 's, all of which have zero amplitudes at the A sites.

3.2 Kagome lattice

We have also considered other lattices with flat bands, such as the kagome lattice in 2D and the sawtooth lattice in 1D. In all cases, we have obtained qualitatively similar results to those for the stub lattice. In this subsection, we present the results for the kagome lattice.

In Fig. 6, we show a sketch of the kagome lattice considered in this paper. The kagome lattice is a triangular lattice with a basis of three inequivalent sites where each lattice site has four nearest neighbors. It is known that the band structure of this lattice consists of two dispersive bands and one flat band. The shape of the lattice depends on the angle ϕ . In

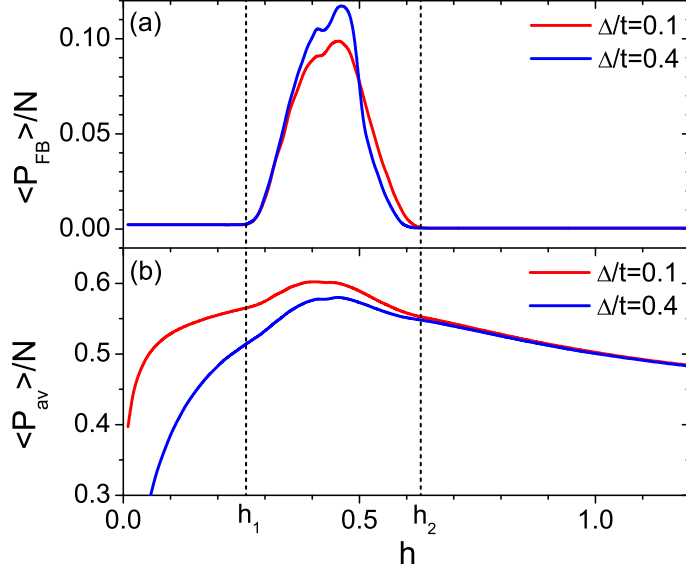


Fig. 4 Normalized participation ratios of a stub lattice averaged over (a) 800 flat-band states and (b) all 2400 states and averaged over 100 different disorder configurations when $N = 2400$ and $\Delta/t = 0.1, 0.4$ plotted versus h . The positions of h_1 and h_2 , between which the delocalization of some flat-band states occurs, are indicated by dashed lines.

the present work, we fix $\phi = 60^\circ$ and then all the nearest neighbor distances are the same and equal to a . For the convenience of numerical calculations, we consider the (conventional) unit cell shown in the orange box. This cell contains six points and six different directions for the nearest-neighbor hopping. We repeat these unit cells N_x and N_y times in the x and y directions respectively. Then the total number of sites N is equal to $6N_xN_y$. The effective Hamiltonian describing the kagome lattice can be written as

$$\mathcal{H} = -\frac{t}{2} \sum_{\langle i,j \rangle} \left(e^{\mathbf{g} \cdot \mathbf{s}_{ij} / \hbar} b_i^\dagger b_j + e^{-\mathbf{g} \cdot \mathbf{s}_{ij} / \hbar} b_j^\dagger b_i \right) + \sum_i v_i b_i^\dagger b_i, \quad (6)$$

where b_i^\dagger and b_i are the creation and annihilation operators at the site i respectively and \mathbf{s}_{ij} denotes the lattice vector directed from the site j to the site i . The notation $\langle i, j \rangle$ denotes that the summation is taken over only the nearest-neighbor sites. \mathbf{g} is an imaginary vector potential and v_i is an on-site random potential chosen from the uniform distribution in $[-\Delta, \Delta]$. We fix the direction of \mathbf{g} so that $\theta = 45^\circ$. Then the quantity $\mathbf{g} \cdot \mathbf{s}_{ij} / \hbar$ takes six different values $\pm h / \sqrt{2}$, $\pm(\sqrt{6} + \sqrt{2})h/4$, and $\pm(\sqrt{6} - \sqrt{2})h/4$ where $h = ga/\hbar$, depending on the choice of \mathbf{s}_{ij} .

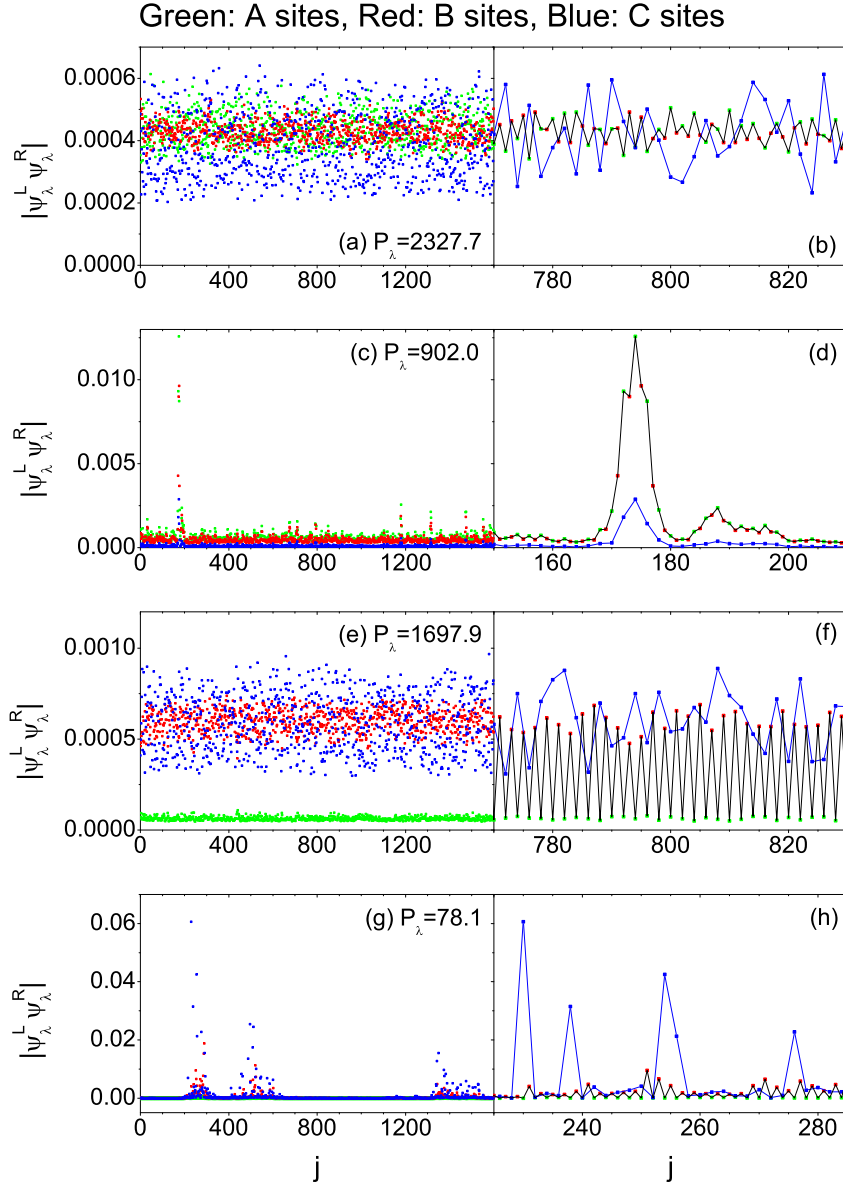


Fig. 5 Local density distributions for (a-d) two typical dispersive-band and (e-h) two typical flat-band states plotted versus j , the odd [even] values of which correspond to the B (red) [A (green) and C (blue)] sites in the same disorder configuration as in Fig. 2, when $N_c = 800$, $\Delta/t = 0.4$, and $h = 0.45$. (b), (d), (f), and (h) are the magnified versions of (a), (c), (e), and (g) respectively. In (a), (c), (e), and (g), P_λ is equal to 2327.7, 902.0, 1697.9, and 78.1 respectively.

In Fig. 7, we show the complex energy spectra of a kagome lattice in a single disorder configuration, when $N_x = N_y = 20$, $N = 6N_xN_y = 2400$, $\Delta/t = 0.1$, and $h = 0.01, 1.1, 1.7$. When h is as small as 0.01, all eigenstates are localized and their eigenvalues are real. In the absence of disorder and the imaginary vector potential, the flat band of the kagome lattice described by Eq. (6) is located precisely at the energy $E = t$. As the disorder is introduced, this band gets broadened. When Δ/t is equal to 0.1, the flat-band states exist roughly in the range of $0.9 < E/t < 1.1$.

As h increases, more and more states become delocalized and take complex energy eigenvalues. At $h = 1.1$, we find that all dispersive-band states are delocalized. Except for a small number of the band-edge states with real eigenvalues, these states have complex eigenvalues as shown in Fig. 7(b). In contrast, however, the flat-band states are only partially delocalized and a substantial portion of them remain localized for all h . An expanded plot of the distribution of the eigenvalues inside the boxed region in Fig. 7(b) is shown in Fig. 7(d). We clearly find that some fraction of the flat-band states are delocalized and the distribution of their eigenvalues is markedly different from that in the dispersive-band case. That most of the states with complex eigenvalues lying close to the real line in the range $0.9 < \text{Re } E_\lambda/t < 1.1$ belong to the flat band is evident from the observation that there is no similar behavior near $-1.1 < \text{Re } E_\lambda/t < -0.9$. As h increases further, the delocalized flat-band states begin to return to compact localized states, similarly to the behavior of the stub lattice which we have described in detail in the main text. When $h = 1.7$, we find that almost all flat-band states are re-localized with real energy eigenvalues.

In the kagome lattice, it is difficult to distinguish the flat and dispersive bands unambiguously and therefore we have not calculated P_{FB} . However, we can observe the influence of the double transition occurring to some flat-band states from the shape of the P_{av} curve. In Fig. 8, we plot the participation ratio of a kagome lattice averaged over all eigenstates in the same disorder configuration as in Fig. 7 when $N_x = N_y = 20$ and $\Delta/t = 0.1$ versus h . We find that this quantity takes a maximum value at $h \approx 1.1$. The appearance of a clear peak of P_{av} as a function of h can be considered as a consequence of the double transition and is fully consistent with the behavior obtained for the stub lattice.

4 Conclusion

In conclusion, we have performed a numerical study of Anderson localization in disordered non-Hermitian lattice models with flat bands. We have found that there appears a double transition from localized to delocalized and back to localized states for a substantial portion of the flat-band states and explored its characteristics in detail. The re-entrant localization

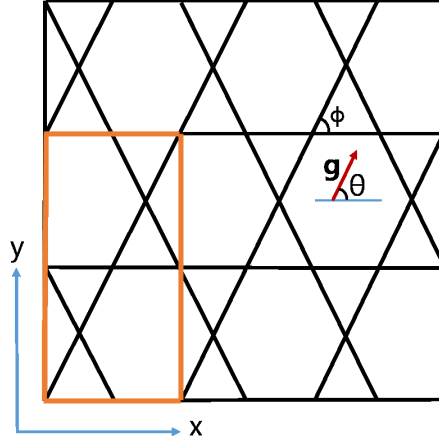


Fig. 6 Sketch of the kagome lattice. The direction of the imaginary vector potential \mathbf{g} is indicated with an arrow. The unit cell considered in the numerical calculation is shown in the orange box.

transition, which is due to the interplay among disorder, non-Hermiticity, and flat band, is a phenomenon occurring in many disordered models with an imaginary vector potential and a flat band.

The predictions made in this study can be readily verified through experiments performed on a variety of systems including ultracold atoms in optical lattices [38], non-Hermitian electric circuit lattices [39], superconducting vortex lattices [40], and synthetic photonic lattices constructed using optical waveguide arrays [41] or arrays of coupled ring resonators [42], where the structures are fabricated to have flat bands. The imaginary vector potential, or equivalently, the nonreciprocal hopping can be realized using methods such as Aharonov-Bohm rings [38, 43] and coupled-resonator optical waveguide structures [20]. Future experimental work in that direction will be of great interest.

Acknowledgment

This research was supported through a National Research Foundation of Korea Grant (NRF-2022R1F1A1074463) funded by the Korean Government. It was also supported by the Basic Science Research Program funded by the Ministry of Education (2021R1A6A1A10044950).

References

- [1] P. W. Anderson, Absence of diffusion in certain random lattices, *Phys. Rev.* **109**, 1492 (1958).
- [2] P. A. Lee and T. V. Ramakrishnan, Disordered electronic systems, *Rev. Mod. Phys.* **57**, 287 (1985).
- [3] F. Evers and A. D. Mirlin, Anderson transitions, *Rev. Mod. Phys.* **80**, 1355 (2008).

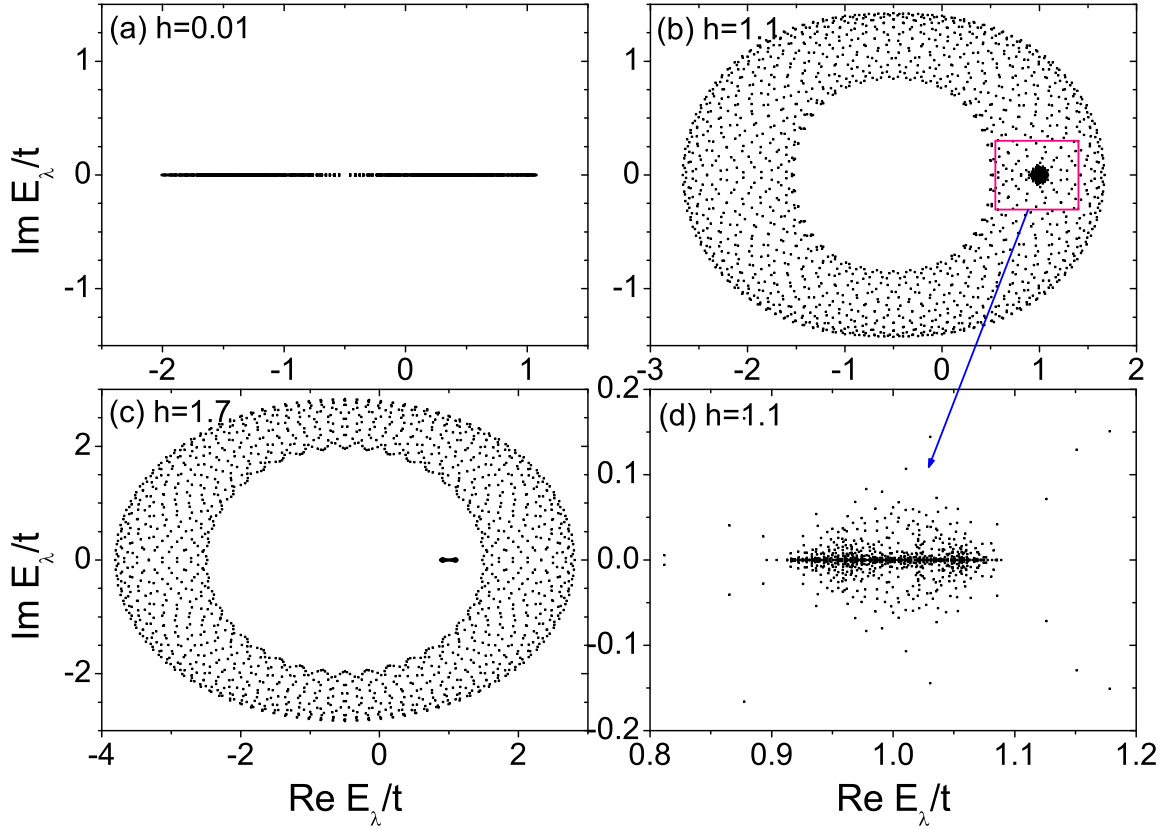


Fig. 7 (a-c) Complex energy spectra of a kagome lattice in a single disorder configuration when $N_x = N_y = 20$, $N = 6N_xN_y = 2400$, $\Delta/t = 0.1$, and $h = 0.01, 1.1, 1.7$. (d) An expanded view of the boxed region in (b).

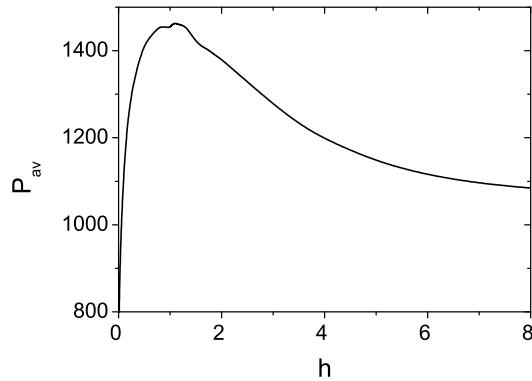


Fig. 8 Participation ratio of a kagome lattice averaged over all 2400 eigenstates in the same disorder configuration as in Fig. 7 when $N_x = N_y = 20$ and $\Delta/t = 0.1$ plotted versus h .

- [4] S. A. Gredeskul, Y. S. Kivshar, A. A. Asatryan, K. Y. Bliokh, Y. P. Bliokh, V. D. Freilikher, and I. V. Shadrivov, Anderson localization in metamaterials and other complex media, *Low Temp. Phys.* **38**, 570 (2012).
- [5] M. Segev, Y. Silberberg, and D. N. Christodoulides, Anderson localization of light, *Nat. Photon.* **7**, 197 (2013).
- [6] I. Yusipov, T. Lapyeva, S. Denisov, and M. Ivanchenko, Localization in open quantum systems, *Phys. Rev. Lett.* **118**, 070402 (2017).
- [7] Y. Sharabi, H. H. Sheinfux, Y. Sagi, G. Eisenstein, and M. Segev, Self-induced diffusion in disordered nonlinear photonic media, *Phys. Rev. Lett.* **121**, 233901 (2018).
- [8] A. Iomin, From power law to Anderson localization in nonlinear Schrödinger equation with nonlinear randomness, *Phys. Rev. E* **100**, 052123 (2019).
- [9] S. Kim and K. Kim, Anderson localization and delocalization of massless two-dimensional Dirac electrons in random one-dimensional scalar and vector potentials, *Phys. Rev. B* **99**, 014205 (2019).
- [10] S. Kim and K. Kim, Anderson localization of two-dimensional massless pseudospin-1 Dirac particles in a correlated random one-dimensional scalar potential, *Phys. Rev. B* **100**, 104201 (2019).
- [11] F. Suzuki, M. Lemeshko, W. H. Zurek, and R. V. Krems, Anderson localization of composite particles, *Phys. Rev. Lett.* **127**, 160602 (2021).
- [12] S. Longhi, Inverse Anderson transition in photonic cages, *Opt. Lett.* **46**, 2872 (2021).
- [13] N. Moiseyev, *Non-Hermitian Quantum Mechanics* (Cambridge University Press, Cambridge, 2011).
- [14] Y. Ashida, Z. Gong, and M. Ueda, Non-Hermitian physics, *Adv. Phys.* **69**, 249 (2020).
- [15] N. Hatano and D. R. Nelson, Localization transitions in non-Hermitian quantum mechanics, *Phys. Rev. Lett.* **77**, 570 (1996).
- [16] N. Hatano and D. R. Nelson, Non-Hermitian delocalization and eigenfunctions, *Phys. Rev. B* **58**, 8384 (1998).
- [17] N. M. Shnerb and D. R. Nelson, Winding numbers, complex currents, and non-Hermitian localization, *Phys. Rev. Lett.* **80**, 5172 (1998).
- [18] K. Kim and D. R. Nelson, Interaction effects in non-Hermitian models of vortex physics, *Phys. Rev. B* **64**, 054508 (2001).
- [19] G. Refael, W. Hofstetter, and D. R. Nelson, Transverse Meissner physics of planar superconductors with columnar pins, *Phys. Rev. B* **74**, 174520 (2006).
- [20] S. Longhi, D. Gatti, and G. Della Valle, Robust light transport in non-Hermitian photonic lattices, *Sci. Rep.* **5**, 13376 (2015).
- [21] S. Longhi, Non-Hermitian bidirectional robust transport, *Phys. Rev. B* **95**, 014201 (2017).
- [22] D. Leykam, A. Andreanov, and S. Flach, Artificial flat band systems: From lattice models to experiments, *Adv. Phys.: X* **3**, 1473052 (2018).
- [23] J. M. Luck, Scaling laws for weakly disordered 1D flat bands, *J. Phys. A: Math. Theor.* **52**, 205301 (2019).
- [24] J.-W. Rhim, K. Kim, and B.-J. Yang, Quantum distance and anomalous Landau levels of flat bands, *Nature* **584**, 59 (2020).
- [25] L. Balents, C. R. Dean, D. K. Efetov, and A. F. Young, Superconductivity and strong correlations in moiré flat bands, *Nat. Phys.* **16**, 725 (2020).
- [26] K. Kim and S. Kim, Mode conversion and resonant absorption in inhomogeneous materials with flat bands, *Phys. Rev. B* **105**, 045136 (2022).
- [27] M. Goda, S. Nishino, and H. Matsuda, Inverse Anderson transition caused by flatbands, *Phys. Rev. Lett.* **96**, 126401 (2006).
- [28] J. T. Chalker, T. S. Pickles, and P. Shukla, Anderson localization in tight-binding models with flat bands, *Phys. Rev. B* **82**, 104209 (2010).
- [29] D. Leykam, S. Flach, O. Bahat-Treidel, and A. S. Desyatnikov, Flat band states: Disorder and nonlinearity, *Phys. Rev. B* **88**, 224203 (2013).
- [30] D. Leykam, J. D. Bodyfelt, A. S. Desyatnikov, and S. Flach, Localization of weakly disordered flat band states, *Eur. Phys. J. B* **90**, 1 (2017).
- [31] P. Shukla, Disorder perturbed flat bands: Level density and inverse participation ratio, *Phys. Rev. B* **98**, 054206 (2018).
- [32] Y. Zong, S. Xia, L. Tang, D. Song, Y. Hu, Y. Pei, J. Su, Y. Li, and Z. Chen, Observation of localized flat-band states in Kagome photonic lattices, *Opt. Express* **24**, 8877 (2016).
- [33] S. Weimann, L. Morales-Inostroza, B. Real, C. Cantillano, A. Szameit, and R. A. Vicencio, Transport in sawtooth photonic lattices, *Opt. Lett.* **41**, 2414 (2016).
- [34] B. Real, C. Cantillano, D. López-González, A. Szameit, M. Aono, M. Naruse, S.-J. Kim, K. Wang, and R. A. Vicencio, Flat-band light dynamics in stub photonic lattices, *Sci. Rep.* **7**, 15085 (2017).
- [35] J. Liu, X. Mao, J. Zhong, and R. A. Römer, Localization, phases, and transitions in three-dimensional extended Lieb lattices, *Phys. Rev. B* **102**, 174207 (2020).

- [36] Z. Gong, Y. Ashida, K. Kawabata, K. Takasan, S. Higashikawa, and M. Ueda, Topological phases of non-Hermitian systems, *Phys. Rev. X* **8**, 031079 (2018).
- [37] T. Yoshida and Y. Hatsugai, Reduction of one-dimensional non-Hermitian point-gap topology by correlations, [arXiv:2205.09333v1](https://arxiv.org/abs/2205.09333v1) (2022).
- [38] W. Gou, T. Chen, D. Xie, T. Xiao, T.-S. Deng, B. Gadway, W. Yi, and B. Yan, Tunable nonreciprocal quantum transport through a dissipative Aharonov-Bohm ring in ultracold atoms, *Phys. Rev. Lett.* **124**, 070402 (2020).
- [39] T. Helbig, T. Hofmann, S. Imhof, M. Abdelghany, T. Kiessling, L. W. Molenkamp, C. H. Lee, A. Szameit, M. Greiter, and R. Thomale, Generalized bulk-boundary correspondence in non-Hermitian topoelectrical circuits, *Nat. Phys.* **16**, 747 (2020).
- [40] R. R. Biswas, Majorana Fermions in vortex lattices, *Phys. Rev. Lett.* **111**, 136401 (2013).
- [41] R. A. Vicencio Poblete, Photonic flat band dynamics, *Adv. Phys.: X* **6**, 1878057 (2021).
- [42] G. Li, L. Wang, R. Ye, S. Liu, Y. Zheng, L. Yuan, and X. Chen, Observation of flat-band and band transition in the synthetic space, *Adv. Photonics* **4**, 036002 (2022).
- [43] H. Li, T. Kottos, and B. Shapiro, Half-period Aharonov-Bohm oscillations in disordered rotating optical ring cavities, *Phys. Rev. A* **94**, 031801(R) (2016).